Spatial coherence of the seismic wavefield continuously recorded by the USArray

L. Seydoux, N. M. Shapiro, J. Rosny, M. Landès

HAL Id: insu-03581296
https://insu.hal.science/insu-03581296

Spatial coherence of the seismic wavefield continuously recorded by the USArray

L. Seydoux[1], N. M. Shapiro[1,2], J. de Rosny[3], and M. Landès[1]

[1]Department of Seismology, Institut de Physique du Globe de Paris, Paris, France, [2]Institute of Volcanology and Seismology FEB RAS, Petropavlovsk-Kamchatsky, Russia, [3]ESPCI Paris, CNRS, Institut Langevin, PSL Research University, Paris, France

Abstract We use a method based on the array covariance matrix eigenvalues to study the level of spatial coherence and of isotropy of the seismic wavefield continuously recorded during 2010 by the USArray. First, we observe that the raw data are often dominated by local sources. To remove their influence, we apply spectral and temporal normalizations to the input signals. We notice that this widely used preprocessing in ambient-noise seismology does not fully homogenize the seismic wavefield and that some strongly coherent arrivals persist. Among these persistent signals generated by teleseismic sources we detect (1) seismic waves emitted by strong earthquakes, (2) a nearly continuous quasi-monochromatic signal at 26 s period, and (3) multiday coherent wave trends in the spectral band of oceanic microseisms (0.07 – 0.2 Hz). For the latter, beamforming analysis shows that while most of the signals are composed of surface waves, some are dominated by body waves likely generated in the deep ocean.

1. Introduction

While seismic noise has long been considered an ultimate barrier to the detailed analysis of seismic signals, it is nowadays widely used in many approaches to image the Earth's structure. These approaches emerged during the latest decade and take benefit of the random and diffuse wavefields. Their main theoretical foundation states that the cross correlations between records from different sensors of a completely random and equipartitioned wavefield converge toward the Green's functions of the media between the sensors [e.g., *Weaver and Lobkis*, 2001; *Campillo and Paul*, 2003; *Snieder*, 2004; *Roux et al.*, 2005; *Gouédard et al.*, 2008]. This results in a possibility to convert seismic receivers recording random wavefields into virtual seismic sources that can, in turn, be used for imaging. This approach is particularly attractive when applied to records of the ambient seismic noise, which is excited by various type of environmental and anthropogenic sources, and which can be recorded at any location. The first demonstrations of the reconstruction of deterministic seismic waves from correlations of ambient seismic noise [*Shapiro and Campillo*, 2004; *Sabra et al.*, 2005a] and their application to the subsurface imaging [*Shapiro et al.*, 2005; *Sabra et al.*, 2005b] have led to a very fast development of seismic imaging and monitoring methods [*Campillo et al.*, 2011] that became today routinely used seismological practices.

The main shortcoming of these methods based on correlations of ambient seismic noise is that the latter is never fully equipartitioned and stationary. It is nonstationary in time and spectral domains and is generated by unevenly distributed seismic sources [e.g., *Stehly et al.*, 2006; *Shapiro et al.*, 2006; *Landès et al.*, 2010; *Ermert et al.*, 2016]. Moreover, continuous seismic records contain pulse-like signals from earthquakes that induce spurious arrivals in the cross correlations [e.g., *Boué et al.*, 2013; *Lin et al.*, 2013]. To compensate for both the wavefield anisotropy and nonstationarity, preprocessing methods including the temporal and the spectral normalization [e.g., *Bensen et al.*, 2007] and/or the data preselection [e.g., *Poli et al.*, 2012] are usually applied to raw seismic records. In many cases, indeed, the amplitude normalization strongly improves the convergence of the cross correlations and leads to a stable extraction of deterministic waves and of their travel times. Nevertheless, even after this normalization, strong imprints of dominant seismic sources may remain in the coherence of the correlated records resulting in imperfect reconstructions of different parts of the Green's functions.

Therefore, a meaningful interpretation of the interstation cross correlation of seismic records requires evaluating the level of isotropy and statistical stationarity of the correlated wavefield. In this study, we apply a recently proposed array-based approach [*Seydoux et al.*, 2016] to 1 year of continuous seismic records by 121 stations

of the USArray Experiment to quantitatively estimate the level of spatial coherence of the seismic wavefield as a function of time and frequency. This method is attractive because of its robustness and because it does not require any prior knowledge on the medium to be used.

The paper is organized as follows. First, we describe the method and give qualitative expectation of its results. Then we introduce the USArray data selected for this study and explain the choice of parameters used to run the method with this data set. We finally present the results obtained during year 2010 from the vertical-component records at frequencies between 0.01 and 1 Hz. The method highlights the limitations of the signal normalization proposed in *Bensen et al.* [2007] by comparing the results obtained from the prepro-cessed and nonpreprocessed data. At frequencies below 0.1 Hz, the teleseismic activity remains visible even after the preprocessing and clearly shows strong short-time increases of spatial coherence. In the secondary microseismic frequency band (between 0.1 and 0.2 Hz), coherent arrivals are observed, particularly during the northern summer. We perform a plane wave beamforming analysis of a typical microseismic event and conclude that it is composed of Rayleigh waves incoming from the south-west of the USArray and is likely generated by the interaction of long-propagating oceanic swells and the continental shores. At ∼0.035 Hz (∼26 s period), a nearly continuous monochromatic coherent signal is observed and our results are compared with previous studies of this phenomenon [*Holcomb*, 1980, 1998; *Shapiro et al.*, 2006]. We also investigate a nondispersive microseismic signal recorded around 1 February and show that it is composed of body waves incoming from south-southwest of the USArray.

2. Method

Seismic arrays have been originally designed in mid-1960s to detect and locate weak seismic sources embed-ded in background noise [see, for example, *Frosch and Green Jr.*, 1966; *Bungum et al.*, 1971]. The beamforming is a typical array processing method where the array covariance matrix is projected onto plane waves (see *Rost* [2002] for a review of array-based techniques in seismology). This approach is robust but relatively basic. Indeed, the geometry of the array and the number of sensors can introduce artifacts. Moreover, the plane wave assumption is not met for sources lying under the array, and finally, the background noise can induce strong fluctuations in the beamforming output.

To overcome these limitations, several classes of high-resolution methods arose [e.g., *Bienvenu and Kopp*, 1980; *Wax et al.*, 1984; *Wax and Kailath*, 1985; *Schmidt*, 1986; *Goldstein and Archuleta*, 1987]. These methods gener-ally aim at separating the signal and noise subspaces (respectively, formed by the signal- and noise-related eigenvalues and eigenvectors) based on the eigendecomposition of the covariance matrix. More generally, the eigenvalues of the covariance matrix estimated from seismic data contain rich information about the level of spatial coherence of the recorded wavefield [*Samson and Olson*, 1980; *Wagner and Owens*, 1996]. Following the method introduced in *Seydoux et al.* [2016], we use the width of distribution of the array covariance matrix eigenvalues as a robust estimation of the level of wavefield spatial coherence.

2.1. Covariance Matrix Estimation
Let $u_i(f, t)$ be the complex Fourier spectrum at frequency f of the time segment of data starting at time t recorded by sensor i over a duration δt. We define the array data vector as

$$\mathbf{u}(f, t) = \left[u_1(f, t), u_2(f, t), \ldots, u_N(f, t) \right]^T, \tag{1}$$

where N is the total number of sensors and T stands for transposition. The array covariance matrix is defined as the average of the cross-spectral matrix $\mathbf{u}(f, t)\mathbf{u}^\dagger(f, t)$ over a set of M half-overlapping time segments of duration δt (i.e., over a duration $\Delta t = (M - 1)\delta t/2$):

$$\mathbf{C}(f, t) = \left\langle \mathbf{u}(f, t)\mathbf{u}^\dagger(f, t) \right\rangle_{\Delta t} = \frac{1}{M} \sum_{m=0}^{M-1} \mathbf{u}(f, t + m\delta t/2)\mathbf{u}^\dagger(f, t + m\delta t/2). \tag{2}$$

2.2. Covariance Matrix Spectral Width
We perform the eigenvalue decomposition of the obtained covariance matrices, in each time window and at each frequency, using the `Eigen v3` C++ Library (G. Guennebaud et al., Eigen v3: C++ template library for linear algebra, 2014, http://eigen.tuxfamily.org). The eigenvalues $\lambda_i(f, t)$ are real and positive because the covariance matrix is inherently Hermitian and positive semidefinite (by definition in equation 2). We sort

them in descending order to obtain the covariance matrix spectrum. The typical width of distribution of the eigenvalues $\sigma(f, t)$ within a given time window starting at time t and at frequency f is given by

$$\sigma(f, t) = \frac{\sum_{i=1}^{N}(i - 1)\lambda_i(f, t)}{\sum_{i=1}^{N} \lambda_i(f, t)} . \tag{3}$$

The rank R of the data covariance matrix is defined by the number of nonzero eigenvalues. The covariance matrix is full rank when it is estimated from a number of time segments larger than the number of sensors ($M > N$), otherwise, it is of rank M. In other words, $R = \min(N, M)$. We then expect the spectral width of the data covariance matrix to depend on the content of the seismic data as follows (see *Seydoux et al.* [2016] for a more detailed description):

1. If the array data only consists of noise that is uncorrelated between each sensors (such as self-sensor noise), the covariance matrix spectral width is large, with an approximative value of $R/2$
2. The time segments that contain a signal relative to a single seismic source will contribute to increase the first eigenvalue, leading to a thinner eigenvalue distribution, hence, to a smaller spectral width.
3. If the array data only consists of ambient seismic noise (a random mixture of propagating waves), the covariance matrix eigenvalue spectrum depends on both the array geometry, the frequency and the number of time segments (this have been investigated with the random matrix theory in *Menon et al.* [2012] and *Gerstoft et al.* [2012]). The covariance matrix spectral width is then expected to vary from 0 at low frequencies to $R/2$ at high frequencies.

Generally speaking, and depending on the mutual contributions of the sources, the seismic noise and the uncorrelated noise, the covariance matrix spectral width σ is close to 0 when a coherent signal is present and is close to a maximal value $\sigma_{\max}$ when seismic noise is recorded. If, in addition, we assume the seismic data to be free from uncorrelated noise, the covariance matrix spectral width gives a robust and quantitative estimation of the level of spatial coherence of the seismic wavefield.

2.3. Plane Wave Beamforming

The aforementioned distribution of the covariance matrix eigenvalues can be used to detect coherent signals but is not sufficient to define their origin. For this second goal, we use the plane wave beamforming analysis (see *Rost* [2002] for a review of beamforming methods). We did not consider any high-resolution methods in the present study, because we did not want to estimate the azimuth and slowness of the seismic waves accurately but just to understand the types of waves involved. The mathematical expression of the plane wave beamforming can be derived by projecting the covariance matrix on the functional subspace formed of plane wave beamformers:

$$\mathbf{b}(f, \gamma, \theta) = \exp(2i\pi f\gamma[\mathbf{x}\cos\theta + \mathbf{y}\sin\theta]) \tag{4}$$

where f is the frequency, γ is the slowness, θ is the back azimuth, and where $\mathbf{x}$ and $\mathbf{y}$ are the vectors of coordinates of the array sensors. The beamforming $\mathbf{B}(f, \gamma, \theta, t)$ is then defined as

$$\mathbf{B}(f, \gamma, \theta, t) = \mathbf{b}^{\dagger}(f, \gamma, \theta)\mathbf{C}(f, t)\mathbf{b}(f, \gamma, \theta) . \tag{5}$$

3. Application to the Transportable Component of the USArray in 2010

We analyze the vertical-component continuous records from the U.S. Transportable Array Experiment (USArray) during the year 2010. We selected the records of 121 stations shown as black triangles in Figure 1a that were operating continuously from 1 January to 31 December.

3.1. Selection of the Parameters

As explained in *Seydoux et al.* [2016], the choice of the subwindow lengths used in equation (2) is constrained by the minimal analyzed frequency and by the maximal travel time spent by the slowest seismic waves to propagate across the network. With the selected seismic array, the largest interstation spacing is about 1200 km. Considering a minimal wave speed of 1.25 km/s, the maximal travel time is of 960 s. We therefore use 960 s long subwindows, giving access to frequencies above ∼0.002 Hz.

The number of subwindows M is related to the convergence of the covariance matrix estimation. In our case, we wanted to estimate the covariance matrix while keeping a maximal temporal resolution. We, therefore, selected 20 overlapping subwindows of width 960 s, leading to a duration of the computational window of
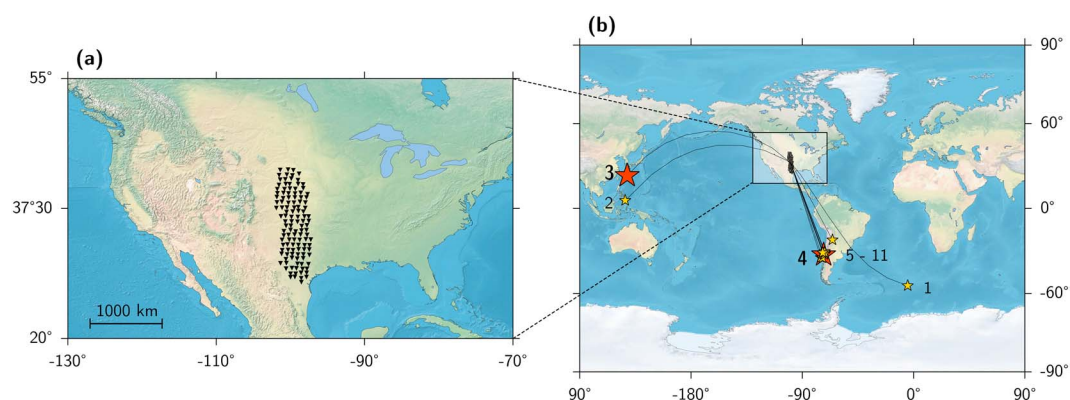
Figure 1. (a) Locations of the 121 seismic stations (black triangles) of the U.S. Transportable Array Experiment that were continuously recording the seismic wavefield from 1 January to 31 December 2010. (b) Epicenters of earthquakes of magnitude higher than 5.3 that occurred between 26 February and 2 March, obtained from the U.S. Geological Survey (USGS) database. Red stars stand for magnitude higher than 7. Numbering indicates the order of occurrence and corresponds to the one used in Figure 3. The great circle path between each epicenter and the center of the USArray is shown in black line.

$\Delta t \approx M\delta t/2 = 20 \times 960/2 = 9600$ s (hence, 2.60 h). With a synthetic test similar to the one described by *Seydoux et al.* [2016], we observe that the covariance matrix spectral width of the isotropic seismic noise varies between 4 at low frequencies ($f = 0.01$ Hz) to 5.5 at frequencies higher than 0.2 Hz (which correspond to $M_{eff}/2$, where M_{eff} is the effective number of overlapping subwindows). We notice that this choice of parameter does not allow to distinguish between uncorrelated noise and seismic noise at frequencies higher than 0.2 Hz. A higher number of subwindows M should be taken into account in this specific goal, with a substantial degradation in the temporal resolution of the analysis. We selected this parameter on purpose, because at the considered frequencies the level of the uncorrelated instrumental noise is expected to be low, and because our main goal is to investigate the presence of coherent seismic sources in the seismic data.

3.2. Results

The covariance matrix spectral width $\sigma(f, t)$ computed from 1 year of raw data is shown in Figure 2a. During most of the time, the seismic wavefield is dominated by apparently coherent signals (with low values of σ) at high and low frequencies. This reflects the fact that the wavefield represented by the ensemble of the continuous raw seismic records by the USArray stations is strongly nonstationary and very far from being equipartitioned. A close inspection of the records shows that most of the low-σ parts of the wavefield correspond to local noise recorded by one or a few closely located stations. The influence of this type of nonstationary signals can be efficiently suppressed with the energy normalization of raw records in time and frequency domain often used in the analysis of the seismic noise cross correlations [e.g., *Bensen et al.*, 2007]. We, therefore, apply this normalization to the ensemble of analyzed records. We start with a time normalization and divide raw traces by the average amplitude computed in a 1.25 s long sliding time window. We then whiten the data spectrum within every Δt window. This is done by dividing the spectra by its amplitude smoothed in 0.8 Hz sliding-frequency window.

The covariance matrix spectral width computed from the normalized seismograms is shown in Figure 2b. Compared to the results obtained from the raw records (Figure 2a), most of the low-sigma parts disappear showing that the preprocessing of individual records, indeed, helps to "homogenize" the wavefield. Nevertheless, some strongly coherent arrivals are still present even after this energy normalization. A more detailed analysis of the main types of signals indicated with white frames in Figure 2b is presented in Figures 3, 4a, 4c, and 4e and is described in the following subsections.

3.3. Observation of the Teleseismic Activity

At frequencies below 0.1 Hz, many short-time drops of the covariance matrix spectral width are observable in Figure 2b, indicating that short-duration coherent signals are detected. These peaks correspond to waves emitted by teleseismic earthquakes. The high-frequency part of this radiation is strongly attenuated and remains visible only for strongest earthquakes.
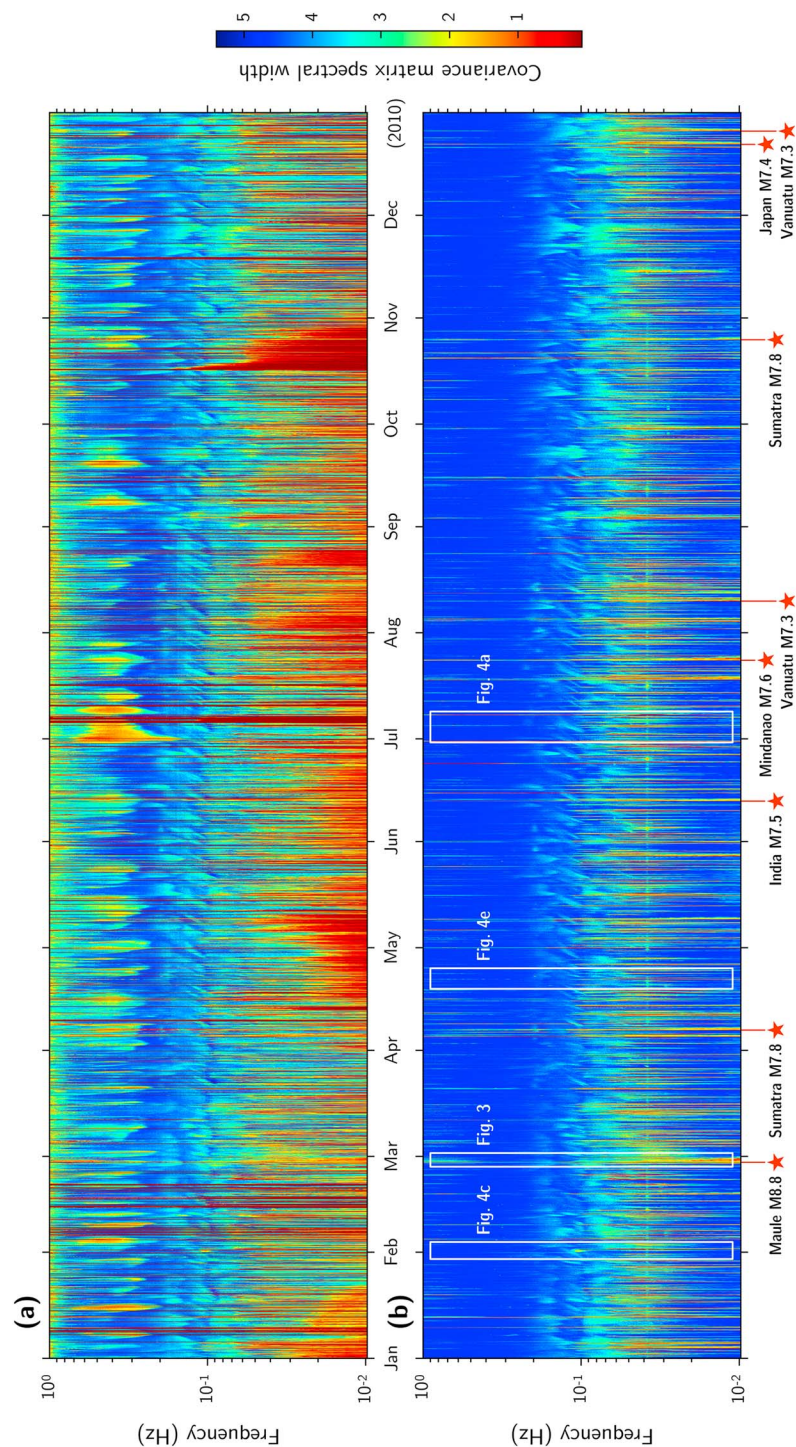
Figure 2. Covariance matrix spectral width versus time and frequency. The color scale indicates the covariance matrix spectral width. Windows where the covariance matrix spectral width is close to 0 contain coherent signals, and windows where the covariance matrix spectral width is close to 5 likely contain incoherent propagating noise. (a) No normalization is applied to the data before computation. (b) Spectral and temporal normalizations are applied to the data before computation. White frames show the time and frequency limits of the zooms in Figures 3, 4a, 4c, and 4e. Red stars indicate the arrival times of Rayleigh waves emitted by $M \geq 7.3$ earthquakes (obtained from the USGS earthquake database).
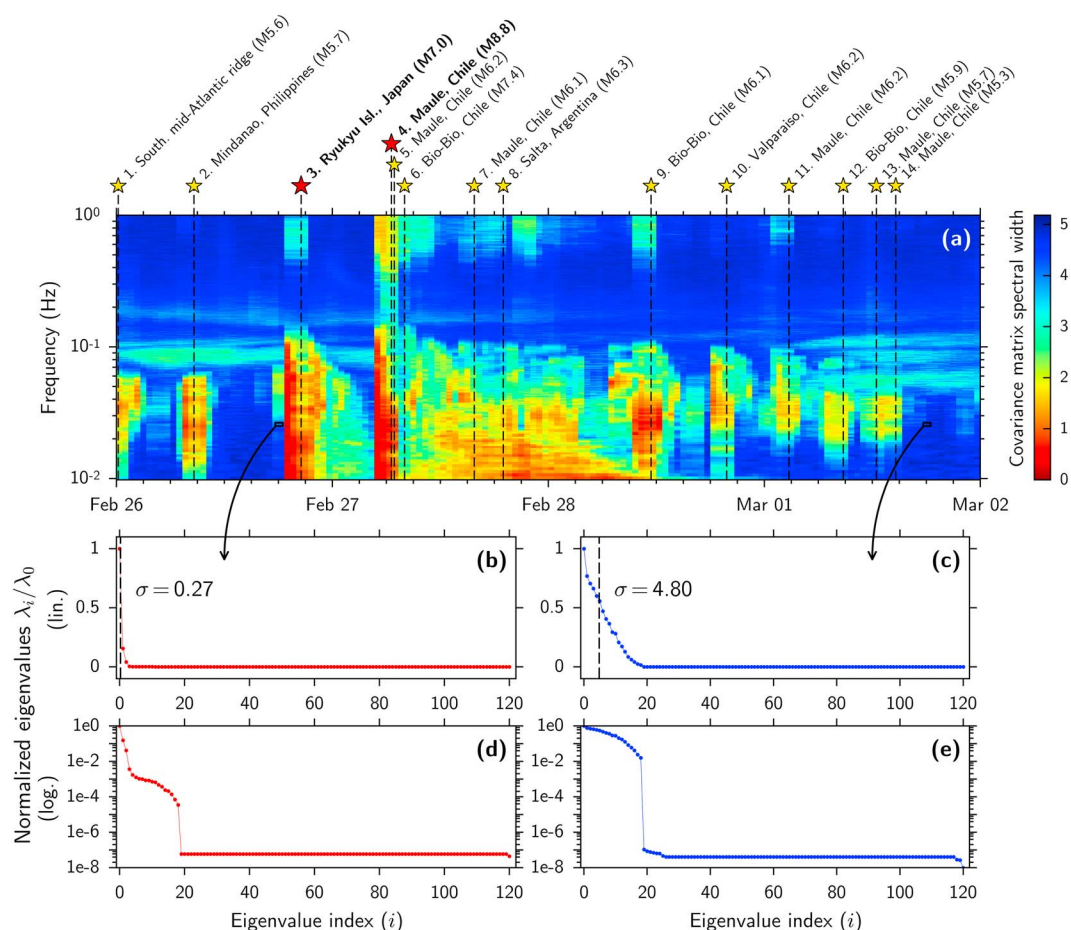
Figure 3. (a) Example of earthquake influence on covariance matrix spectral width obtained from data normalized with the process proposed in *Bensen et al.* [2007]. Earthquakes names are given with their corresponding magnitude; the related epicenters and great circle paths are reported on the global map shown in Figure 1b. (b) Covariance matrix spectrum of the M7.0 Ryukyu Islands earthquake, at 0.25 Hz. (c) Covariance matrix spectrum taken in a time window when coherent event occurs, at 0.25 Hz. (d and e) Covariance matrix spectra (Figures 3b and 3c) with logarithmic y axis scale.

A typical example of earthquake-related signals is shown in Figure 3. In order to illustrate the relationship of the covariance matrix spectral width with the wavefield coherence, two examples of the covariance matrix spectra are provided in Figures 3b and 3c. The covariance matrix spectrum obtained from a time window when the M7.0 Ryukyu Islands earthquake occurred and at 0.25 Hz (Figure 3b) shows up to be dominated by the first eigenvalue, in contrast with the covariance matrix spectrum obtained in a window that looks free from any coherent signal (Figure 3c). The values of the corresponding spectral width are given in each case. Also, the eigenvalues are represented with logarithmic scale in Figures 3d and 3e.

The analyzed window shown in Figure 3 contains several events including the $M = 8.8$ Maule megathrust earthquake that occurred near the coast of central Chile [*Delouis et al.*, 2010]. The arrival times of the Rayleigh waves from the earthquakes of magnitude higher than 5.3 are indicated with black dashed lines in the figure (only the ones with magnitude higher than 6 are indicated within the 24 h after the main shock of the Maule earthquake in order not to saturate the figure). The corresponding epicenter locations and the great circle path of Rayleigh waves are shown in Figure 1b. The extended duration of the earthquake-related drops of σ is explained by the 9600 s long windows used in the computation. All seismic events are clearly distinguishable as low-sigma ($\lesssim 1$) vertical bars at frequencies below 0.1 Hz. For strongest events, the increase of coherence is also observed at high frequencies. So far, the $M = 8.8$ Maule earthquake appears to be highly coherent at all frequencies between 0.01 and 1 Hz. Moreover, it is followed by more than 24 h of coherent coda whose duration is clearly increasing with decreasing frequencies. The long-period coda remains observable over longer time periods because of the slower attenuation of long-period seismic waves within the Earth.
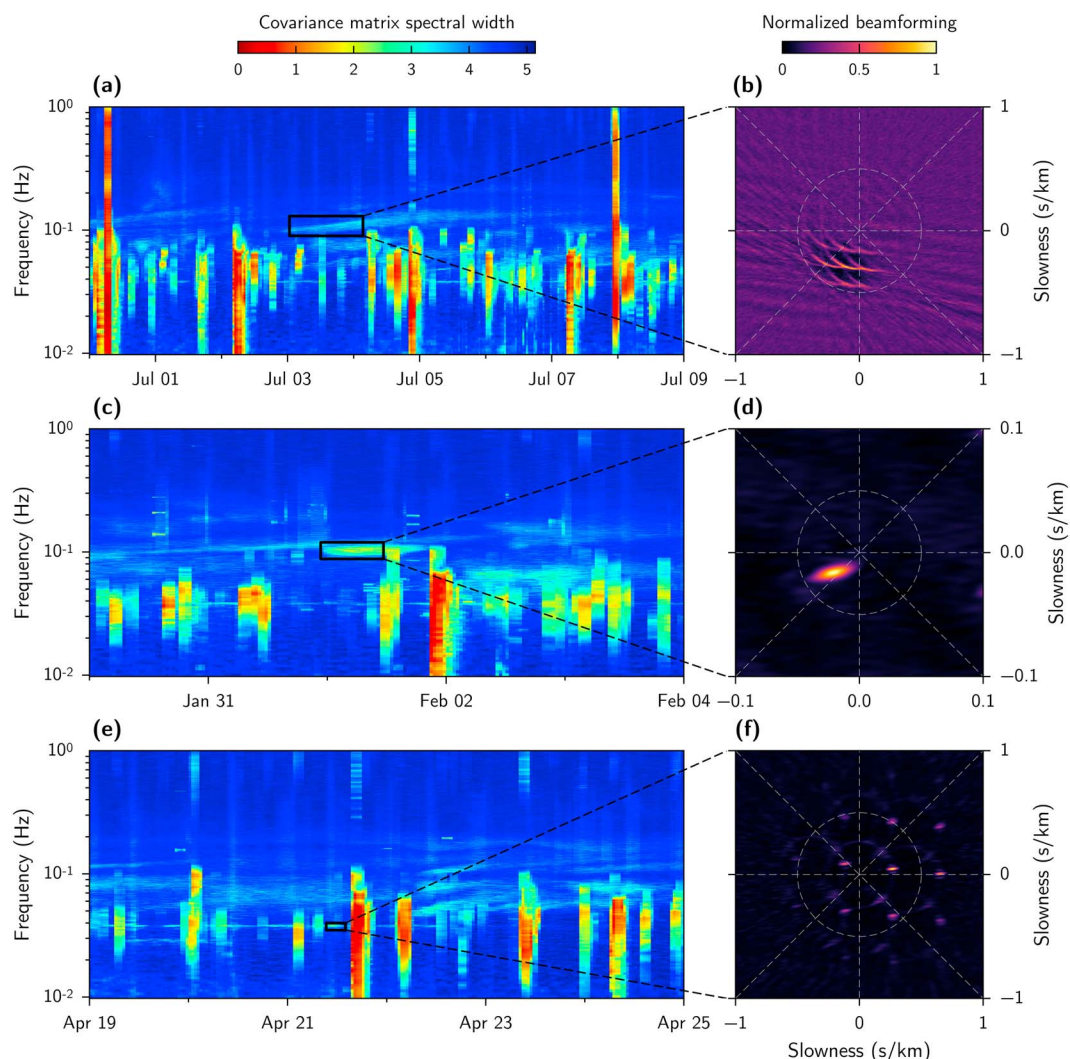
Figure 4. (a, c, e) Zooms of the covariance matrix spectral width obtained from the preprocessed data (Figure 2b). (b, d, f) Plane wave beamforming analyses obtained from the average of the covariance matrix in the time and frequency limits delimited by the respective black frames on the left parts. Dispersive signal analyzed in Figure 4b as Rayleigh waves incoming from between 175 and 225° with a slowness of ~0.34 s km^{-1} (Figure 4a). Nondispersive signal corresponding to Figure 4d body waves incoming from about 230° with a slowness of 0.0269 km s^{-1} (Figure 4c). The 5 h long portion of the nearly continuous and quasi-monochromatic signal (Figure 4e), composed of Rayleigh waves and incoming from 80° of azimuth (Figure 4f).

3.4. Microseismic Noise: Surface Waves Generated by Swells

At frequencies between 0.09 and 0.2 Hz, which correspond to the secondary ocean-generated microseismic band, the covariance matrix spectral width presented in Figure 2b shows many arrivals with increased coherence. Typical characteristics of these signals are their relatively long durations (a few days) and their dispersion with higher frequencies arriving after the low frequencies. A typical example of such dispersive arrival is shown in Figure 4a.

We apply the plane wave beamforming analysis described in section 2.3 to the covariance matrix averaged in time and frequency: between 0.09 and 0.12 Hz and over the whole day of 2010/07/04 (Figure 4b). The beamforming output shows aliasing artifacts because of the short wavelength of the incoming waves compared to the interstation spacing. The location and shape of the principal lobe, however, indicate that the waves are incoming from the south-southwest of the USArray (with an azimuth between 175 and 225°). The estimated slowness is about 0.34 s km^{-1} and corresponds to a Rayleigh wave.

Considering the provenance and the dispersive nature of the signal analyzed in Figure 4b, the most plausible explanation of its origin is that it was generated in vicinity of the coast of Mexico by the nonlinear interaction of an incoming oceanic swell with a relatively shallow near-coastal seafloor [e.g., *Bromirski et al.*, 2013] and then propagates as Rayleigh waves from the coast to the USArray. The long signal duration and visible dispersion is produced by the slowly propagating oceanic swell, whose source is somewhere far from the coast in the Pacific Ocean.

3.5. Microseismic Noise: Teleseismic *P* Waves

While many signals detected in the frequency band between 0.1 and 0.2 Hz are dispersive and correspond to surface waves generated by distant swells, some of them have different properties. As an example, we show in Figure 4c the analysis of a signal recorded during 1 February 2010. This signal is very different from the microseisms generated by distant swells, i.e., it is not dispersive and its frequency range (0.09–0.12 Hz) remains constant. The plane wave beamforming analysis of this signal (Figure 4d) shows a clear maximum with a back azimuth of ~230° and a slowness of ~0.027 km s^{-1}, corresponding to teleseismic *P* waves. A more detailed study of this event has been reported by *Retailleau* [2015] who demonstrated that the *P* waves have been generated by the nonlinear interaction of oceanic wave from a strong storm occurred in the Indian Ocean.

3.6. The 26 s Microseism

Another remarkable feature seen in Figure 2b is a nearly constantly present monochromatic signal (horizontal line) at frequencies about 0.034 Hz (nearly 26 s period). This signal corresponds to previously reported "26 s microseism" [e.g., *Holcomb*, 1980, 1998; *Shapiro et al.*, 2006]. The beamforming analysis of a portion (5 h) of this signal presented in Figure 4f shows a typical aliased pattern corresponding to surface (Rayleigh waves), and its main lobe indicates a back azimuth of ~80° and a slowness of ~0.27 s km^{-1}, which is in perfect agreement with the known source of this microseism in the Gulf of Guinea.

4. Conclusions

We studied the spatial coherence of the seismic wavefield recorded during 1 year (2010) by 121 stations of the transportable component of the USArray. For this goal, we applied the recently developed method [*Seydoux et al.*, 2016] that analyzes the distribution of the eigenvalues of the array covariance matrix and use its "spectral width" to characterize the level of coherence of the recorded wavefield. This method is attractive for its robustness to separate coherent information from the background seismic noise, and also because no prior knowledge on the underlying medium is required to be applied.

We first see that the raw record is strongly nonstationary in time and frequency (Figure 2a). The preprocessing technique proposed in *Bensen et al.* [2007] normalizes the energy of individual records, reducing the influence of strongest parts of the signal (Figure 2a).

At the same time, normalization technique widely used in the data preprocessing for computing noise cross correlations is not sufficient to fully homogenize the recorded wavefield, and, even after applying the normalization, the covariance matrix (and by consequence the cross correlations) contains clear imprints of many different sources. In particular, the influence of the strongest earthquakes on the cross correlation of continuous records cannot be ignored. Also, multiple surface and body wave signals emitted by microseismic sources remain clearly visible.

An important consequence of the presented observations is that the cross correlations of the continuous seismic records computed with the recently developed methods of the signal preprocessing cannot be considered as correlations of the equipartitioned wavefield and are not exact proxies of the Earth's Green's functions (especially for amplitudes). Therefore, the inhomogeneous source distribution must be taken into account when interpreting these cross correlations.

References

Bensen, G. D., M. H. Ritzwoller, M. P. Barmin, A. L. Levshin, F. Lin, M. P. Moschetti, N. M. Shapiro, and Y. Yang (2007), Processing seismic ambient noise data to obtain reliable broad-band surface wave dispersion measurements, *Geophys. J. Int.*, *169*(3), 1239–1260.

Bienvenu, G., and L. Kopp (1980), Adaptivity to background noise spatial coherence for high resolution passive methods, in *IEEE International Conference on Acoustics, Speech, and Signal Processing (ICASSP 1980)*, pp. 307–310, IEEE, Denver, Colo.

Boué, P., P. Poli, M. Campillo, H. Pedersen, X. Briand, and P. Roux (2013), Teleseismic correlations of ambient seismic noise for deep global imaging of the Earth, *Geophys. J. Int.*, *194*(2), 844–848.

Bromirski, P. D., R. A. Stephen, and P. Gerstoft (2013), Are deep-ocean-generated surface-wave microseisms observed on land?, *J. Geophys. Res. Solid Earth*, *118*, 3610–3629, doi:10.1002/jgrb.50268.

Bungum, H., E. S. Husebye, and F. Ringdal (1971), The NORSAR array and preliminary results of data analysis, *Geophys. J. Int.*, *25*(1–3), 115–126.

Campillo, M., and A. Paul (2003), Long-range correlations in the diffuse seismic coda, *Science*, *299*(5606), 547–549.

Campillo, M., P. Roux, and N. M. Shapiro (2011), Seismic, Ambient Noise Correlation, in *Encyclopedia of Solid Earth Geophysics*, pp. 1230–1236, Springer, Dordrecht, Netherlands.

Delouis, B., J.-M. Nocquet, and M. Vallée (2010), Slip distribution of the February 27, 2010 $M_w = 8.8$ Maule earthquake, central Chile, from static and high-rate GPS, InSAR, and broadband teleseismic data, *Geophys. Res. Lett.*, *37*, L09309, doi:10.1029/2011GL047065.

Ermert, L., A. Villaseñor, and A. Fichtner (2016), Cross-correlation imaging of ambient noise sources, *Geophys. J. Int.*, *204*(1), 347–364.

Frosch, R. A., and P. E. Green Jr. (1966), The concept of a large aperture seismic array, *Proc. R. Soc. A*, *290*, 368–384.

Gerstoft, P., R. Menon, W. S. Hodgkiss, and C. F. Mecklenbräuker (2012), Eigenvalues of the sample covariance matrix for a towed array, *J. Acoust. Soc. Am.*, *132*(4), 2388–2389.

Goldstein, P., and R. J. Archuleta (1987), Array analysis of seismic signals, *Geophys. Res. Lett.*, *14*(1), 13–16.

Gouédard, P., et al. (2008), Cross-correlation of random fields: Mathematical approach and applications, *Geophys. Prospect.*, *56*(3), 375–393.

Holcomb, G. L. (1980), Microseisms: A twenty-six-seconds spectral line in long period Earth motion, *Bull. Seismol. Soc. Am.*, *70*(4), 1055–1070.

Holcomb, L. G. (1998), Spectral structure in the Earth's microseismic background between 20 and 40 seconds, *Bull. Seismol. Soc. Am.*, *88*(3), 744–757.

Landès, M., F. Hubans, N. M. Shapiro, A. Paul, and M. Campillo (2010), Origin of deep ocean microseisms by using teleseismic body waves, *J. Geophys. Res.*, *115*, B05302, doi:10.1029/2009JB006918.

Lin, F.-C., D. Li, R. W. Clayton, and D. Hollis (2013), High-resolution 3D shallow crustal structure in Long Beach, California: Application of ambient noise tomography on a dense seismic array, *Geophysics*, *78*(4), Q45–Q56.

Menon, R., P. Gerstoft, and W. S. Hodgkiss (2012), Asymptotic eigenvalue density of noise covariance matrices, *IEEE Trans. Signal Process.*, *60*(7), 3415–3424.

Poli, P., H. A. Pedersen, M. Campillo, and the POLENET/LAPNET Working Group (2012), Noise directivity and group velocity tomography in a region with small velocity contrasts: The northern Baltic shield, *Geophys. J. Int.*, *192*(1), 413–424.

Retailleau, L. (2015), Seismic wavefield analysis using antenna processing on USArray, PhD thesis, Institut de Physique du Globe, Paris, France.

Rost, S. (2002), Array seismology: Methods and applications, *Rev. Geophys.*, *40*(3), 1008–27.

Roux, P., K. G. Sabra, W. A. Kuperman, and A. Roux (2005), Ambient noise cross correlation in free space: Theoretical approach, *J. Acoust. Soc. Am.*, *117*(1), 79–84.

Sabra, K. G., P. Roux, and W. A. Kuperman (2005a), Emergence rate of the time-domain Green's function from the ambient noise cross-correlation function, *J. Acoust. Soc. Am.*, *118*(6), 3524–3531.

Sabra, K. G., P. Gerstoft, P. Roux, W. A. Kuperman, and M. C. Fehler (2005b), Surface wave tomography from microseisms in Southern California, *Geophys. Res. Lett.*, *32*, L14311, doi:10.1029/2005gl023155.

Samson, J. C., and J. V. Olson (1980), Some comments on the descriptions of the polarization states of waves, *Geophys. J. Int.*, *61*(1), 115–129.

Schmidt, R. O. (1986), Multiple emitter location and signal parameter estimation, *IEEE Trans. Antennas Propag.*, *34*(3), 276–280.

Seydoux, L., N. M. Shapiro, J. de Rosny, F. Brenguier, and M. Landès (2016), Detecting seismic activity with a covariance matrix analysis of data recorded on seismic arrays, *Geophys. J. Int.*, *204*(3), 1430–1442.

Shapiro, N. M., and M. Campillo (2004), Emergence of broadband Rayleigh waves from correlations of the ambient seismic noise, *Geophys. Res. Lett.*, *31*, L07614, doi:10.1029/2004GL019491.

Shapiro, N. M., M. Campillo, L. Stehly, and M. H. Ritzwoller (2005), High-resolution surface-wave tomography from ambient seismic noise, *Science*, *307*, 1615–1618.

Shapiro, N. M., M. H. Ritzwoller, and G. D. Bensen (2006), Source location of the 26 sec microseism from cross-correlations of ambient seismic noise, *Geophys. Res. Lett.*, *33*, L18310, doi:10.1029/2006GL027010.

Snieder, R. (2004), Extracting the Green's function from the correlation of coda waves: A derivation based on stationary phase, *Phys. Rev. E*, *69*(4), 46610.

Stehly, L., M. Campillo, and N. M. Shapiro (2006), A study of the seismic noise from its long-range correlation properties, *J. Geophys. Res.*, *111*, B10306, doi:10.1029/2005JB004237.

Wagner, G. S., and T. J. Owens (1996), Signal detection using multi-channel seismic data, *Bull. Seismol. Soc. Am.*, *86*(1A), 221–231.

Wax, M., and T. Kailath (1985), Detection of signals by information theoretic criteria, *IEEE Trans. Acoust. Speech*, *33*(2), 387–392.

Wax, M., T. J. Shan, and T. Kailath (1984), Spatio-temporal spectral analysis by eigenstructure methods, *IEEE Trans. Acoust. Speech*, *32*(4), 817–827.

Weaver, R. L., and O. I. Lobkis (2001), Ultrasonics without a source: Thermal fluctuation correlations at MHz frequencies, *Phys. Rev. Lett.*, *87*(13), 134,301.1–134,301.4.